INL/JOU-19-52525-Revision-0

Nondestructive characterization of polycrystalline 3D microstructure with time-domain Brillouin scattering

David H Hurley, Zilong Hua

June 2019

INL/JOU-19-52525-Revision-0

Nondestructive characterization of polycrystalline 3D microstructure with time-domain Brillouin scattering

David H Hurley, Zilong Hua

June 2019

Idaho National Laboratory
Idaho Falls, Idaho 83415

http://www.inl.gov

Prepared for the
U.S. Department of Energy
Office of Nuclear Energy
Under DOE Idaho Operations Office
Contract DE-AC07-05ID14517

Nondestructive characterization of polycrystalline 3D microstructure with time-domain Brillouin scattering

Yuzhou Wang, David H. Hurley, Zilong Hua, Gaofeng Sha, Samuel Raetz, Vitalyi E. Gusev, Marat Khafizov**

Y. Wang, Dr. G. Sha, and Prof. M. Khafizov*,
Department of Mechanical and Aerospace Engineering,
The Ohio State University,
Columbus, OH 43210, USA

Dr. D. H. Hurley* and Dr. Z. Hua
Idaho National Laboratory,
P.O. Box 1625,
Idaho Falls, ID 83415, USA

Dr. V. E. Gusev and Dr. S. Raetz
Laboratoire d'Acoustique de l'Université du Maine (LAUM),
UMR-CNRS 6613, Le Mans Université, Avenue Olivier Messiaen, 72085 Le Mans, France

Corresponding authors: David Hurley, Tel: 1 (208) 526-3665, E-mail: david.hurley@inl.gov and Marat Khafizov, Tel: 1 (614) 292-2544, E-mail: Khafizov.1@osu.edu

Abstract

We employ gigahertz frequency ultrasonic waves to non-invasively image grain microstructure in polycrystalline ceria, an important electrolyte material for solid oxide fuel cells. This technique, termed time domain Brillouin scattering (TDBS), is a pump-probe technique that launches and monitors ultrasonics waves as they propagate from the surface into the depth of a sample. We demonstrate the capability of TDBS to image surface and subsurface grain structure by measuring mode and depth dependent velocity of the ultrasonic wave. A neural network tool is adopted to determine grain orientation from measured velocities. The TDBS results compare closely with electron backscatter diffraction (EBSD) measurements. This work expands the application of picosecond ultrasonics to three-dimensional imaging and offers a new route for the nondestructive microstructure characterization and in situ examination of polycrystalline materials.

1. Introduction

Grain boundaries serve an important role in defining the physical properties of ceramic materials used in the energy industry[1]. For example, ion transport in solid oxide fuels is affected by atomic segregation at grain boundaries[2]. Grain boundaries can also significantly impact thermal transport in materials used for thermal management as well as high burnup nuclear fuels[3-6]. In addition, mechanical properties of energy materials are often influenced by the diffusion of atoms in high stress and high temperature environments[7, 8]. Grain boundaries, under these extreme conditions can act as barriers or provide a pathway for atomic diffusion[9, 10]. Many of the above mentioned phenomena are strongly influenced by the local environment around grain boundaries[11].

Many new characterization techniques have aided in the investigation of the influence of grain boundaries on materials properties. These include the study of grain morphology using electron backscatter diffraction coupled with serial sectioning, the mapping of space charge fields using Kelvin probe forced microscopy, and the study of local chemistry using electron energy loss spectroscopy and atom probe tomography[12-14]. While these characterization techniques are noteworthy in that they provide spatially resolved information of individual boundaries, they either require specially prepared samples using focused ion beam milling or are only sensitive to surface structure.

Laser ultrasonics presents an appealing alternative as it can be used to perform volumetric materials characterization without material removal. Examples include biological imaging of living cells, depth profiling in nanoporous films, seismic tomography, and the distribution of irradiation damage in epitaxial defined interfaces [15-20]. For the application to grain boundaries, an ultrasonic wave is subjected to reflection and transmission due to abrupt changes in directionally dependent elastic properties associated with grain boundaries [19, 21]. Consequently, by analyzing the acoustic signals one can obtain quantitative information on the subsurface grain structure. This new characterization approach has recently been demonstrated using picosecond duration acoustic pulses to image texture in polycrystalline ice [22, 23]. This technique, termed time domain Brillouin scattering (TDBS), involves generating and detecting high-frequency ultrasonic waves propagating in the depth direction of transparent or semitransparent materials. Changes in the character of the ultrasonic waves can be directly attributed to elastic inhomogeneity. Using TDBS to characterize grain boundaries is still in the very early stages of development and holds great promise to image 3D grain boundary structure.

In this report, we present our work on the imaging of grain orientation and location of subsurface grain boundaries in polycrystalline ceria using TDBS. Ceria is an important electrolyte material used in solid oxide fuel cells due to its ability to transport oxygen and protons [24]. Its ionic conductivity is improved by optimal doping and can be further increased through grain boundary engineering where certain dopants enhance oxygen transport across or along the grain boundaries[25]. Probing grain boundaries in ceria presents an excellent test case for TDBS. It has already been shown that TDBS can effectively probe local chemistry and defect structure at interfaces by tuning the probe to a photon energy just below the bandgap[26]. Simultaneous imaging of subsurface grain structure would expand the capability of TDBS. With this aim, we use TDBS to obtain a contour map of ultrasonic wave velocity with high contrast on a polycrystalline ceria sample. An inverse algorithm based on neural networks is applied to obtain a grain orientation map from the measured Brillouin frequency map. The results are compared to images obtained from electron backscatter diffraction (EBSD) analysis. Additionally, subsurface grain structure is constructed in 3D based on time windowed analysis of the TDBS results.

2. Time-domain Brillouin Scattering

Principles of TDBS

TDBS uses an ultra-short laser pulse (pump) to excite longitudinal and shear polarized ultrasonic waves[27-29]. Ultrasonic pulse generation is accomplished by either irradiating a semiconductor with an ultrashort pump pulse comprised of above bandgap energy photons or irradiating a transparent substrate that is coated with a thin metallic transducer film. The ultrasonic waves travel in the depth direction normal to the sample surface, with a nanometer scale wavelength. The lateral width of the generated acoustic beams is controlled by optical focusing of the pump laser and sub-micrometer resolution can be achieved with high magnification objectives. The velocity of the ultrasonic pulses depends on the elastic stiffness tensor and the crystallite orientation. A second ultrashort laser pulse (probe), typically derived from the same pump laser pulse, is used to detect ultrasonic waves as they propagate in the depth direction of the sample. The interaction of the probe beam with the ultrasonic wave is governed by photoelastic coupling[19, 30, 31]. There are two reflected probe beams, one from the free surface of the sample and one that is reflected from the strain field of the propagating ultrasonic pulse. These two beams interfere resulting in oscillatory features in time resolved reflectivity signal whose period is determined by the time it takes the acoustic wave to propagate half the optical wavelength of the probe beam. For the case where the probe light and acoustic pulses are collinear, the oscillation frequency given by

(1)

where *n* is refractive index at probe's wavelength and *v* is speed of acoustic mode. TDBS has been previously applied to characterize aspects of surface and subsurface grain structure [16, 32]. It has also been suggested that if the elastic stiffness tensor components are known, TDBS could be used to measure grain orientation[16].

Experiment

The experiment setup uses a femtosecond Ti:sapphire laser (Coherent Mira 900), with pulse width of 130 fs and repetition rate of 76 MHz for acoustic phonon generation and detection[33, 34]. The output wavelength can be tuned from 700 nm to 980 nm depending on the sample optical property. After exiting the aperture, a portion of the laser pulse is frequency doubled by sending it through a beta phase barium borate crystal. In our case, the output photon energy is tuned close to ceria bandgap energy for stronger photoelastic coupling (2.92 eV). The probe and pump beams are separated by a dichroic beam splitter. The probe beam (410 nm) is sent through a mechanical delay stage and is used to make long temporal scans (up to several ns). The pump beam at 820 nm is modulated by an AOM (acousto-optic modulator) with frequency of 100 kHz to increase the signal-to-noise ratio via the application of the lock-in detection. A mechanical shaker is employed in the pump leg and is used for alignment and for collecting short temporal scans (<350 ps). Fast data acquisition speed of the shaker makes it suitable for grain orientation imaging at the surface, however for depth resolved profiling, we apply the delay stage to monitor acoustic wave propagation over a longer delay time. Powers of both beams are adjusted by optical attenuators and a half-wave plate is employed in the probe leg to rotate their polarization. A 50× microscope objective is used to focus both the pump and probe beams onto the sample surface. The spot size of both beams is approximately 2 μm.

A polycrystalline ceria sintered pellet was purchased from AlfaAesar. The pellet was annealed at 1500 for 4 hours to promote grain growth. After annealing the average grain size measured using EBSD is approximately 30 μm. The sample is mirror polished and coated with approximately 20 nm of gold. The thin gold film aids in the generation of longitudinal ultrasonic waves at the film surface and provides a method for shear wave generation due to mode conversion at the film sample interface. The deposition of transducer thin film to enhance shear phonons has been successfully applied to ZnO and Zn[31, 35].

The sample was placed on 2D translation stage controlled by a computer. A TDBS oscillation frequency map is obtained by raster scanning with 2 µm step. At each point the signal is averaged over 50 times to improve signal to noise ratio, which takes about 30 seconds. The thermal background is subtracted from the TDBS signal and a Fourier transform is taken to determine oscillation frequencies at each point.

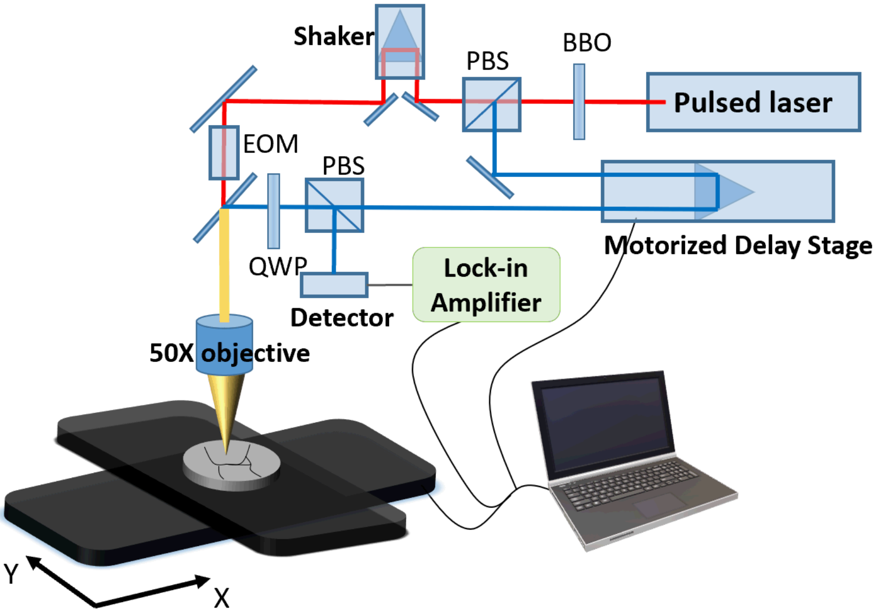

Figure 1. A schematic of the TDBS apparatus. (BBO: Beta Barium Borate nonlinear optical crystal; PBS: polarizing beam splitter; EOM: electro-optical modulator; QWP: quarter wave plate)

The sound velocity is calculated by solving the Christoffel equation [16, 36]. It is based on the solution of constitutive equation of motion *for* plane bulk acoustic wave defined in the form *along* a particular crystal orientation. In general, the crystal orientation relative to the sample surface is defined by three Euler angles. It is more convenient to define grain orientation using Miller indices based on crystal plane (hkl) and crystal axis [uvw], defining surface normal and roll directions, respectively[37]. For a grain of a material with cubic symmetry whose surface normal is defined by normalized orientation (*), the sound velocities are* obtained by evaluating the eigenvalues of matrix *A* given by

(2)

where *i, j*=13, *C* are the elastic tensors, is density, and *V* is acoustic velocity [16].

3. Results

3.1 Surface grain orientation

The reflectivity transient on a ceria grain with orientation defined by (hkl) = (-3,2,10) is shown in Fig.2a. The thermal background has been subtracted to accentuate the oscillation portion of the signal. The signal reveals a strong oscillation component stemming from the longitudinal mode and a smaller amplitude shear oscillation at approximately half the longitudinal frequency. Fig.2b depicts the Fourier transform of the transient shown in Fig.2a. The center frequency of the longitudinal mode (LA mode) is 93.6 GHz that of the shear mode (TA) is 44.9 GHz. The oscillation amplitude remains relatively constant up to 300 ps, indicating negligible optical and acoustic attenuation. The former is consistent with the fact that the probe wavelength is slightly smaller than bandgap energy of ceria. For the current grain and others listed in Table 1, typically only one shear mode is observed. This is partially attributed to the shear strain amplitudes. Two transmitted strains have quite different amplitudes and naturally one with the larger amplitude manifests itself in the signal. On the other hand, probe polarization can also influence shear mode amplitude[38]. We observed that shear mode amplitude changed with the probe beam polarization, and even diminished at certain angles. Further discussion falls out of the scope of this work and will be addressed in the future.

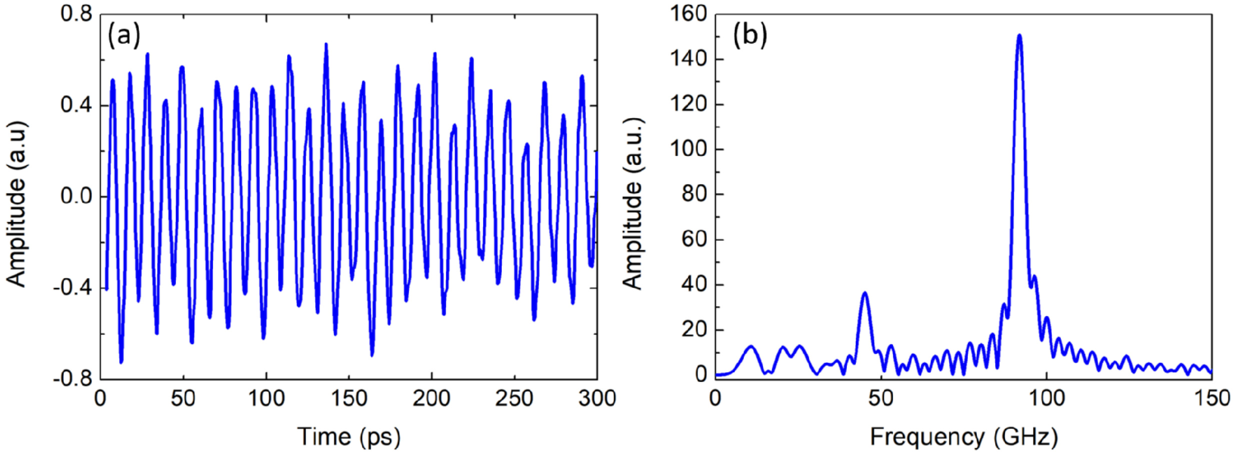

Figure 2. Brillouin oscillation observed on the surface of grain (-3,2,10) in (a) time and (b) frequency domain

Next, we used the same setup to image the structure of a subsurface grain boundary. This imaging is based on the principle that when the acoustic wave travels from one grain to another with a different orientation, the ultrasonic velocity changes. In Fig.3, we plot the experiment data (blue line) and compare it to a sine wave that is fitted to the first few cycles of the experimental data (red line). Because the transmitted acoustic wave travels at a different velocity after entering the second crystallite, the measurement starts to deviate from the fitted sine wave around 130 ps. This is confirmed as we fit the data after this time to a sine wave of different frequency (green line). Using EBSD, the orientation dependent phonon velocity is obtained by solving the Christoffel equation introduced above. This information can in turn be used to extract the location of the subsurface grain boundary. For the case shown in Fig.3, the boundary is located approximately 0.9 μm beneath the surface.

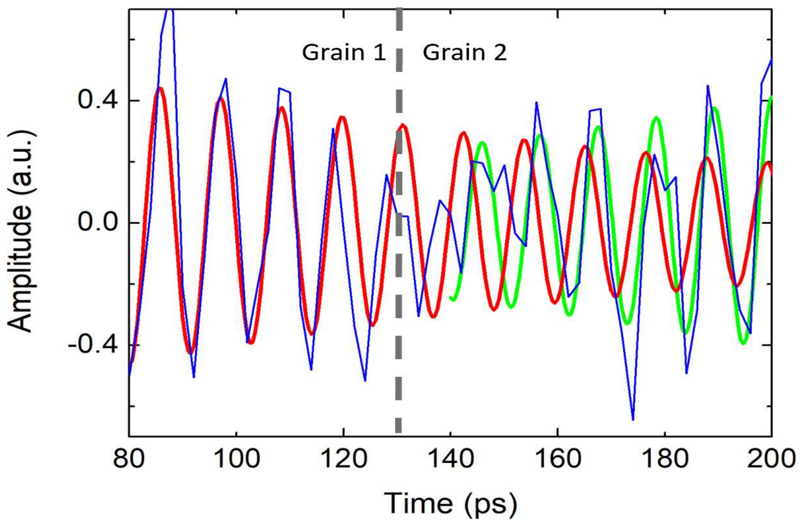

Figure 3. Example of transient reflectivity signal near a grain boundary; (blue) experimental data; (red) sine fitting to the first few cycles of experimental data; (green) sine fitting to the experimental data after grain boundary. Grey dash line represents the location of grain boundary.

In order to precisely determine the grain orientation, a prior knowledge of single crystal elastic constants is needed. The single crystal elastic constants of ceria have been determined experimentally by two studies using inelastic neutron scattering (INS) and Brillouin scattering (BS)[39, 40]; however, these two measurements are notably different. The experimental frequencies measured in several grains are given in Table 1. Model frequencies were calculated using Eq. (1) and Eq. (2) where grain orientations were obtained from EBSD and elastic constants from INS. The refractive index, 2.5, was independently measured using optical ellipsometry. The fitted elastic constants, obtained by minimizing the difference between the measured and calculated frequencies, are compared with literature values in Table 2.

Table 1. Summary of Brillouin frequency on ceria grains

(hkl)/ letters denote grain position in Fig. 4	(0,0,1)/A	(-2,3,17)	(-1,8,26)	(-3,2,10)/D	(10,5,24)	(-20,1,22)	(12,-8,17)
	[13,1,0]	[27,-16,6]	[26,0,1]	[10,10,1]	[10,4,-5]	[18,-14,17]	[11,8,-4]
exp. freq. (GHz)	99.1	96.6	94.2	93.6	93.4	88.8	88.1
(LA and TA, error is 1 GHz)	na	41.4	47.5	44.9	48.3	na	54.8
model freq. (GHz)	96.4	95.0	93.5	92.5	90.4	84.0	83.1
(liter. elastic tensor)	34.3	37.2	41.6	41.5	45.8	58.3	53.5

Table 2. Elastic tensor of ceria

Method	(GPa)	(GPa)	(GPa)	Zener ratio
INS [39]		117	57	0.34
BS [40]	403	105	60	0.40
Current work		136	71	0.42

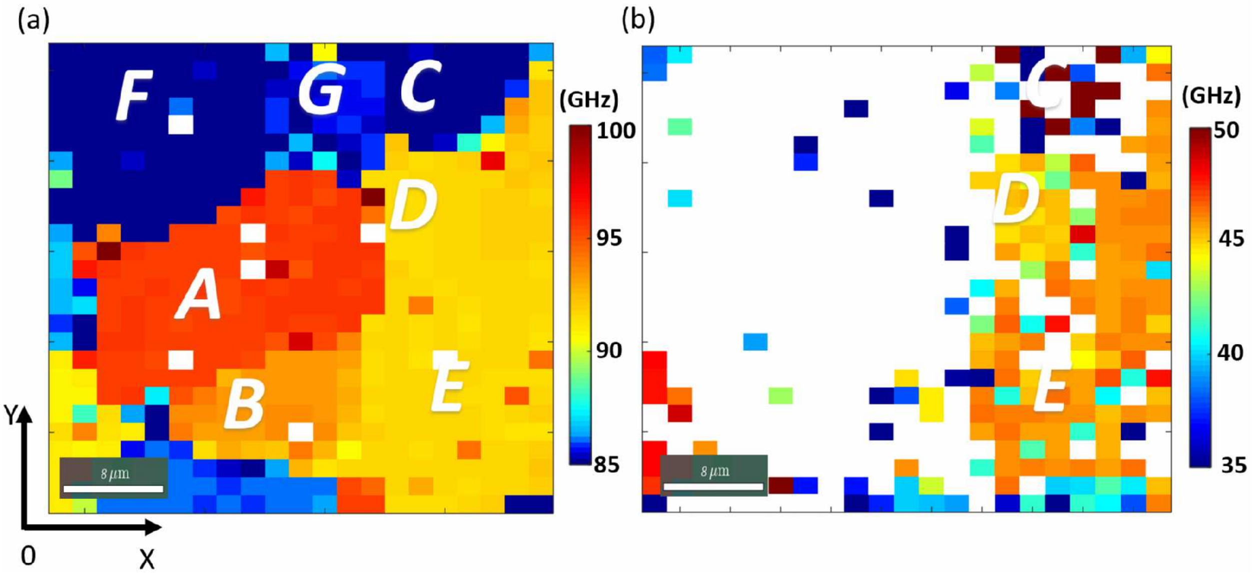

Figure 4. (a) Longitudinal mode frequency imaging on polycrystalline ceria; (b) shear mode frequency imaging on the same area. Pixel size is 2 μm.

We performed TDBS measurement on the surface of ceria sample. Fig.4 presents a result of a raster scan over an area 40 X 50 μm^2 with step of 2 μm. The color represents the Brillouin frequency value of a longitudinal mode (LA) in Fig.4a and of a shear mode in Fig.4b. In Fig.4a the highest frequency of longitudinal mode is close to 100 GHz, while the lowest is approximately 85 GHz. For the shear mode in Fig.4b, the highest frequency is around 50 GHz, and the lowest is approximately 35 GHz. It is noted that there are many points where the shear mode is not generated with sufficient amplitude to determine its oscillation frequency (blank space). The longitudinal mode map provides consistent color contrast, making it more convenient for grain identification. While the shear mode map has considerably more noise, it can provide additional contrast not visible in the longitudinal mode mapping.

From the longitudinal mode map, it is straightforward to identify the large quadrilateral grain A, corresponding to a grain with an orientation close to (001) as revealed by EBSD in Fig.5a. This grain has the largest LA mode oscillation frequency in the scanned area and this frequency has relatively consistent value across the grain area. Since grain A is aligned along a high symmetry direction, no shear mode is generated. The FFT of the transient signal collected at most locations in this area (Fig.4b) show no prominent shear mode peaks for constructing shear frequency map and therefore are marked in white color by default. On the top section of the scan, there are three smaller grains C, F, and G whose orientations are close to each other but resolvable in EBSD image in Fig.5a. However the contrast between these adjacent grains is barely distinguishable in LA mode map as thedifference in frequency of LA modes are comparable to the frequency resolution of the current setup. In contrast, in the shear mode map, grain C on the top right corner is easily identified as the in general shear modes provide larger contrast. Below the (001) grain, there is a triangular grain B, which also can be discerned from the longitudinal map (Fig.4a) but doesn't generate detectable shear mode. In general, as long as adjacent grains have large enough difference in the Brillouin frequency, the TDBS can provide sufficient contrast to identify grains and determine their dimension. Additionally, the shear mode map can provide decisive information for cases where the contrast in the longitudinal map is low.

Inverse problem

To obtain grain orientation from Brillouin oscillation frequencies, we apply a fitting algorithm basedneural network toolbox available in MATLAB[41]. Artificial neural network was chosen over traditional direct comparison of experiment to the model defined by Eq. 2 as it offered a simpler solution pathway to overcome some technical challenges associated with the development of direct inversion algorithm. One of the challenges is that the simplified analysis captured by model in Eq. 2 is not suitable to determine which of the two shear modes is expected to be most pronounced.. Moreover, the same toolbox can be utilized again to other measurements if the material remains the same. The neural network toolbox comprises a series of processing neurons which are connected by transfer functions and associated with weights[42]. After imputing the data, the output of network is compared with the target data and based on the errors, the weights are continuously adjusted to minimize the error. The current network has three hidden layers and one output layer. To train the network, we generate around 5000 sets of data by sampling a spectrum of orientations and calculating the Brillouin frequency from Eq.(2). 70% of the data is used for training, and the rest is equally divided between validation and testing set. In principle, one could also use experimental data for training but limited number of experimental results prevented us from following this approach. The Brillouin frequencies of LA and TA modes are the input data while orientation is the output data. We employ Levenberg-Marquardt for the training algorithm. Overall, we obtain an R-value of 0.95 with satisfactory accuracy.

Orientation imaging

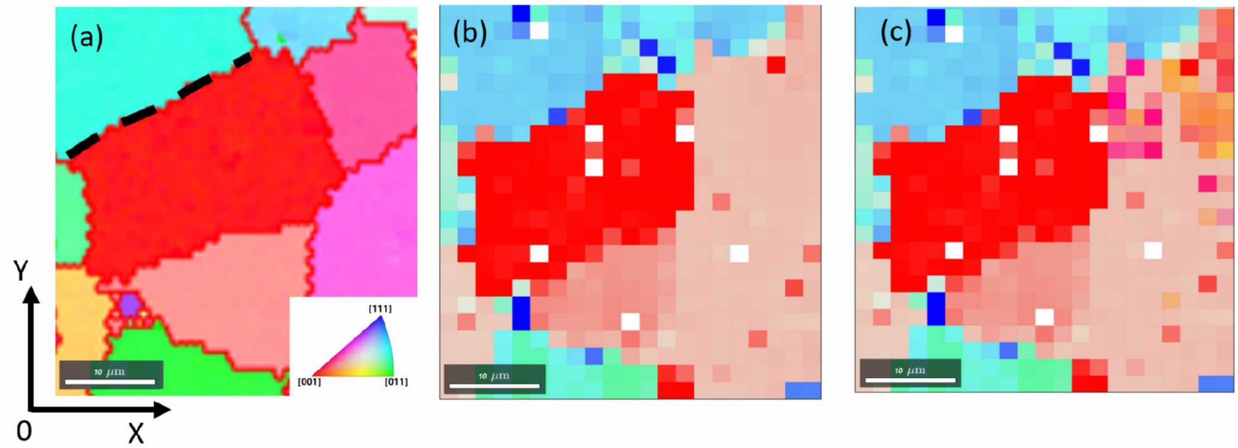

Figure 5. (a) EBSD on the measurement area (b) Inverse pole figure calculated from longitudinal Brillouin frequency (c) Inverse pole figure calculated from longitudinal and shear Brillouin frequency. All figures share the same color key.

Based on the inversion method proposed in the preceding section and experimental oscillation frequency data in Fig.4, the inverse pole figure is derived and plotted in Fig.5b and 5c. The result from TDBS agrees well with the EBSD measurement (Fig.5a) with respect to color presentation (orientation). All the grains preserve their dimension in the inverse pole figure from TDBS. Two rightmost grains D and E which have very close orientations, (-3,2,10) and (-10,7,25), however, are not distinguishable based on LA mode (Fig.5b) for their frequencies are too close to resolve. The orientation angle difference between these two grains is about 6.2. But if we take shear mode into consideration and incorporate it to the neural network, the distinctive features in the orientations are clearly visible in Fig.5c. Their different shear Brillouin frequencies (Fig.4b) help improve the angular resolution to resolve different grains. This underlines the importance of shear waves in the TDBS imaging which has been mostly neglected in previous studies.

3.2 Subsurface imaging

Next, we discuss noninvasive determination of a subsurface location of a grain boundary using the TDBS technique. This approach has been previously applied on polycrystalline UO_2 but was limited to a line scan on the surface to reveal 2D slice of a subsurface grain boundary[16]. Here, we further extend the technique to reconstruct the 3D profile of the grain boundary, whose location is marked in Fig.5a as black dash line. The grain boundary separates grains A and F, with orientations (001) and (19,-7,20), respectively.

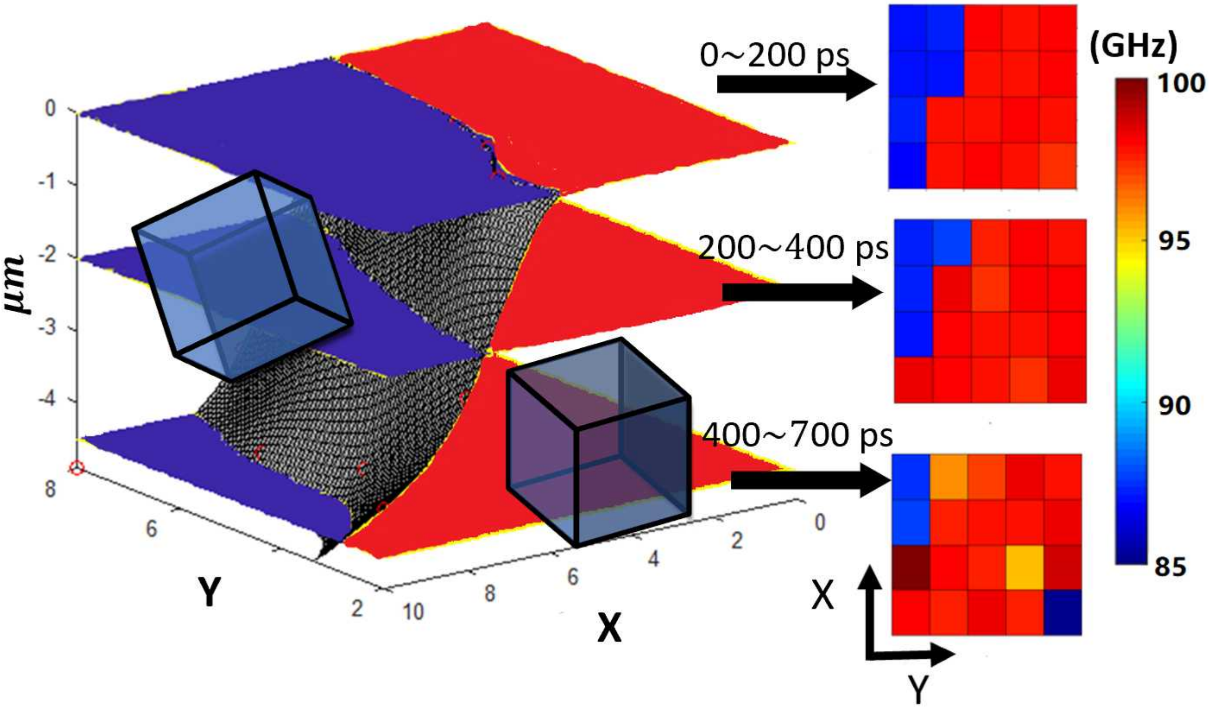

Figure 6. (left) Grain boundary reconstructed in 3D (grey surface); the position of the grain boundary is marked in black dash line in Fig.5(a). Rotated cubes represent grain orientations. (right) fast Fourier transform (FFT) in different delayed time windows and corresponding frequency colorbar.

Unlike the results of the previous section utilizing fast acquisition based on short delay shaker limiting interrogation depth to under 1 μm, here we use a mechanical delay stage which allows the efficient probing down to a depth of 6 μm. Initial signature of the grain boundary at particular location is manifested in the frequency spectrum when two prominent LA modes of comparable amplitude are visible. A time domain signal acquired at each location on the surface was analyzed in 200 ps long window sections. An FFT of each window is taken and LA mode frequency is used to construct the 3D image of grain orientation. Exact location of the boundary can be determined with greater precision if a sine function fitting procedure is applied. [16] The frequency anomaly at bottom right corner of the third section is attributed to another grain boundary. Approximating the grain boundary by a plane, the angle between the boundary and sample surface is found to be 63°.

Now that we have determined the structure of the grain boundary, the impact of acoustic reflection and refraction of the ultrasonic waves at this boundary can be evaluated according to a model of an oblique incidence wave on a plane interface between two half-space anisotropic media[43, 44]. After taking account of the orientations of these two ceria grains (red and blue regions in Fig.5b), it is found that for this specific case the energy reflection coefficient on the boundary is about 8% while most of the acoustic energy (~92%) is transmitted across the grain boundary. Additionally, the deflection angle caused by acoustic velocity mismatch between these two grains is about 6°. The impact of the acoustic refraction is on the measured LA frequency is estimated to be less than 0.5% well below the resolution of the current setup to be detectable. Similarly, the reflected beam has low intensity but is estimated to be propagating parallel to the surface after reflection making in impractical to detect in this configuration.

4. Discussion

In this section, we discuss the spatial resolution and the ability to resolve grains with different orientations of the TDBS. The lateral spatial resolution of TDBS is determined by the spot size and step size of the positioning stage. While the latter is controlled by the positioning accuracy of the translation stage, the probe spot size is limited by optical diffraction. For current probe wavelength of 410 nm and objective numerical aperture of 0.35, the theoretical resolution is estimated to be 580 nm. However pushing to a smaller beam size has its disadvantages, as it brings up other issues like damage of the sample surface anddiffraction of the ultrasonic wave. 3D analysis assumes plane wave propagation of the acoustic wave. Ultrasonic diffraction causes the acoustic wave to spread in dimension, or in other words increases the waist of the strain profile[45-47]. The acoustic spreading deteriorates the lateral imaging resolution of subsurface features as too much energy is lost on the path. Neighboring structures may affect the signal as acoustic waves spread large enough to interact with them. However, the manifestation of these diffractions is taking place at the scale of the Rayleigh length which is much larger than grain size. To quantitatively describe the acoustic beam size, we adopt the equation , where is strain profile waist along depth z, is the initial waist value defined by the pump beam size, and *is the* elasticity-modified acoustic Rayleigh length, *is* the characteristic acoustic wavelength (equals optical wavelength divided by twice the refractive index) and *p* is phonon focusing factor [46]. For our pump size of 2 um, the acoustic beam waist will spread by 10% after travelling 35 m. For the beam waist to grow comparable to grain size (), the travelling distance needs to exceed 1 mm, which is much larger than our grain size. Therefore, it is safe for us to neglect both acoustic diffractions in this work. Generally, the optimal spot size is a tradeoff between accuracy, acquisition time, and sample property.

The ability to precisely evaluate the ultrasonic velocity through frequency measurement ultimately determines the ability to detect grains of different orientation. The frequency resolution is determined by the length of measurement time, *T*, over which the data is collected. To enhance the capability of discerning two close peaks in the Fourier spectrum, the measurement time needs to be increased. The data acquisition time is determined by the synchronization of the lock-in time constant with the motion of the mechanical stage, which is limited by the mechanical movement speed. Further improvement can be achieved by utilizing asynchronous optical sampling (ASOPS) technique, which has been developed to measure ultrafast dynamics[48]. The setup uses two pulse laser of slightly different repetition rate to achieve time-domain sampling. There is no moving part in it and it can improve the acquisition speed by several orders of magnitudes. The utility of ASOPS can also improve lateral resolution by sparing the trouble of laser beam defocusing as well as beam movement on the sample surface as light path is slightly changed with the moving delay stage. This technique will be applied to TDBS in the future to improve measurement resolution.

Zener ratio is a parameter used to describe the elastic anisotropy of cubic crystals. For isotropic materials, , and the surface of velocity for longitudinal and shear mode is a sphere. This means we cannot determine the grain orientation from acoustic velocity. Luckily all single crystals are elastically anisotropic[49] and our technique could apply universally. The amplitude value of , on the other hand, impacts the measurement precision of grain orientations. For materials with farther away from unity, adjacent grains would produce larger contrast in the Brillouin frequency imaging. In the case of ceria with =0.42 and 2 GHz frequency resolution, the adjacent grains have to be at least 14.6 apart in the orientation to be resolvable. If we assume another imaginary material with the same and but half the , the resulting is 0.21. In this case is farther from unity, and the angle resolution is reduced to 13. The above calculation illustrates how Zener ratio influences the angular resolution. The actual angles will depend on the grain orientation. In general, high elastic anisotropy favors the TDBS imaging.

5. Conclusions

In conclusion, we have implemented laser-based Brillouin scattering to image the 3D grain microstructure in polycrystalline ceria. TDBS technique was employed over an area capturing several grains. We determine the grain orientation pole figure from the Brillouin frequency map by adopting a neural network toolbox. For the first time shear acoustic mode is incorporated to improve contrast. Subsurface grain boundary is located by depth resolved frequency profile of Brillouin oscillation. The results show good agreement with EBSD analysis and limitations of the technique's spatial and orientation resolution are discussed. This approach complements the EBSD technique, but unlike EBSD offers opportunity to study subsurface microstructure non-destructively and makes it attractive for in-situ studies and offers opportunities in understanding behavior of polycrystalline materialsfor a range of applications.

Acknowledgement

References

1. Sutton, A.P.B., R. W., *Interfaces in Crystalline Materials (Monographs on the Physics and Chemistry of Materials)*. 1995, Oxford Oxford University Press.
2. Mogensen, M., N. Sammes, and G. Tompsett, *Physical, chemical and electrochemical properties of pure and doped ceria.* Solid State Ionics, 2000. **129**(1-4): p. 63-94.
3. Khafizov, M., et al., *Thermal Conductivity in Nanocrystalline Ceria Thin Films.* Journal of the American Ceramic Society, 2014. **97**(2): p. 562-569.
4. Cahill, D., et al., *Nanoscale thermal transport.* Journal of Applied Physics, 2003. **93**(2): p. 793-818.
5. Ronchi, C., et al., *Effect of burn-up on the thermal conductivity of uranium dioxide up to 100.000 MWdt(-1).* Journal of Nuclear Materials, 2004. **327**(1): p. 58-76.
6. Wang, Z., et al., *Thermal Conductivity of Nanocrystalline Silicon: Importance of Grain Size and Frequency-Dependent Mean Free Paths.* Nano Letters, 2011. **11**(6): p. 2206-2213.
7. Heitjans, P. and S. Indris, *Diffusion and ionic conduction in nanocrystalline ceramics.* Journal of Physics-Condensed Matter, 2003. **15**(30): p. R1257-R1289.
8. Meyers, M., A. Mishra, and D. Benson, *Mechanical properties of nanocrystalline materials.* Progress in Materials Science, 2006. **51**(4): p. 427-556.
9. Andersson, D., et al., *Multiscale simulation of xenon diffusion and grain boundary segregation in UO2.* Journal of Nuclear Materials, 2015. **462**: p. 15-25.
10. Shrader, D., et al., *Ag diffusion in cubic silicon carbide.* Journal of Nuclear Materials, 2011. **408**(3): p. 257-271.
11. Taheri, M., et al., *Site-specific atomic scale analysis of solute segregation to a coincidence site lattice grain boundary.* Ultramicroscopy, 2010. **110**(4): p. 278-284.

12. Dillon, S.J. and G.S. Rohrer, *Characterization of the Grain-Boundary Character and Energy Distributions of Yttria Using Automated Serial Sectioning and EBSD in the FIB.* Journal of the American Ceramic Society, 2009. **92**(7): p. 1580-1585.
13. Leendertz, C., et al., *Evaluation of Kelvin probe force microscopy for imaging grain boundaries in chalcopyrite thin films.* Applied Physics Letters, 2006. **89**(11): p. 113120.
14. Browning, N.D., H.O. Moltaji, and J.P. Buban, *Investigation of three-dimensional grain-boundary structures in oxides through multiple-scattering analysis of spatially resolved electron-energy-loss spectra.* Physical Review B, 1998. **58**(13): p. 8289-8300.
15. Lin, H.N., R.J. Stoner, and H.J. Maris, *Nondestructive testing of microstructures by picosecond ultrasonics.* Journal of Nondestructive Evaluation, 1990. **9**(4): p. 239-246.
16. Khafizov, M., et al., *Subsurface imaging of grain microstructure using picosecond ultrasonics. Acta Mater.*, 2016. **112**: p. 209-215.
17. Perez-Cota, F., et al., *High resolution 3D imaging of living cells with sub-optical wavelength phonons.* Scientific Reports, 2016. **6**.
18. Baydin, A., et al., *The photoelastic coefficient P12 of H+ implanted GaAs as a function of defect density.* Scientific Reports, 2017. **7**(1).
19. Gusev, V.E. and P. Ruello, *Advances in applications of time-domain Brillouin scattering for nanoscale imaging.* Applied Physics Reviews, 2018. **5**(3): p. 031101.
20. Virieux, J. and S. Operto, *An overview of full-waveform inversion in exploration geophysics.* Geophysics, 2009. **74**(6): p. WCC1-WCC26.
21. Graff, K.F., *Wave Motion in Elastic Solids*. 1991, New York: Dover Publications.
22. Nikitin, S.M., et al., *Revealing sub-μm and μm-scale textures in H2O ice at megabar pressures by time-domain Brillouin scattering.* Scientific Reports, 2015. **5**: p. 9352.
23. Kuriakose, M., et al., *Longitudinal sound velocities, elastic anisotropy, and phase transition of high-pressure cubic H 2 O ice to 82 GPa.* Physical Review B, 2017. **96**(13): p. 134122.
24. Godickemeier, M. and L. Gauckler, *Engineering of solid oxide fuel cells with ceria-based electrolytes.* Journal of the Electrochemical Society, 1998. **145**(2): p. 414-421.
25. Lin, Y., et al., *Enhancing grain boundary ionic conductivity in mixed ionic–electronic conductors.* Nature Communications, 2015. **6**: p. 6824.
26. Yarotski, D., et al., *Characterization of irradiation damage distribution near TiO2/SrTiO3 interfaces using coherent acoustic phonon interferometry.* Applied Physics Letters, 2012. **100**(25): p. 251603.
27. THOMSEN, C., et al., *SURFACE GENERATION AND DETECTION OF PHONONS BY PICOSECOND LIGHT-PULSES.* Phys. Rev. B, 1986. **34**(6): p. 4129-4138.
28. THOMSEN, C., et al., *COHERENT PHONON GENERATION AND DETECTION BY PICOSECOND LIGHT-PULSES.* Physical Review Letters, 1984. **53**(10): p. 989-992.
29. Ruello, P. and V. Gusev, *Physical mechanisms of coherent acoustic phonons generation by ultrafast laser action.* Ultrasonics, 2015. **56**: p. 21-35.
30. Matsuda, O., et al., *Fundamentals of picosecond laser ultrasonics.* Ultrasonics, 2015. **56**: p. 3-20.
31. Hurley, D.H., et al., *Laser picosecond acoustics in isotropic and anisotropic materials.* Ultrasonics, 2000. **38**(1): p. 470-474.
32. Lejman, M., et al., *Giant ultrafast photo-induced shear strain in ferroelectric BiFeO3.* Nature Communications, 2014. **5**: p. -.
33. Hurley, D. and K. Telschow, *Simultaneous microscopic imaging of elastic and thermal anisotropy.* Phys. Rev. B, 2005. **71**(24): p. 241410.
34. Khafizov, M. and D. Hurley, *Measurement of thermal transport using time-resolved thermal wave microscopy.* J. Appl. Phys., 2011. **110**(8).
35. Pezeril, T., et al., *Generation and detection of plane coherent shear picosecond acoustic pulses by lasers: Experiment and theory.* Physical Review B, 2007. **75**(17): p. 174307.
36. Li, W., et al., *Determination of crystallographic orientation of large grain metals with surface acoustic waves.* Journal of the Acoustical Society of America, 2012. **132**(2): p. 738-745.
37. Crampin, S., *An introduction to wave propagation in anisotropic media.* Geophysical Journal of the Royal Astronomical Society, 1984. **76**(1): p. 17-28.
38. Matsuda, O., et al., *Coherent shear phonon generation and detection with ultrashort optical pulses.* Physical Review Letters, 2004. **93**(9).
39. CLAUSEN, K., et al., *INELASTIC NEUTRON-SCATTERING INVESTIGATION OF THE LATTICE-DYNAMICS OF THO2 AND CEO2.* Journal of the Chemical Society-Faraday Transactions Ii, 1987. **83**: p. 1109-1112.
40. NAKAJIMA, A., A. YOSHIHARA, and M. ISHIGAME, *DEFECT-INDUCED RAMAN-SPECTRA IN DOPED CEO2.* Physical Review B, 1994. **50**(18): p. 13297-13307.
41. The MathWorks, I., *MATLAB and Neural Network Toolbox Release 2015b*. 2015: Natick, Massachusetts, United States.
42. Hagan, M.T., H.B. Demut, and M. Beale, *Neural network design*. 1st ed. 1996, Boston, MA , USA: PWS Publishing Co. .
43. MANDAL, B., *REFLECTION AND TRANSMISSION PROPERTIES OF ELASTIC-WAVES ON A PLANE INTERFACE FOR GENERAL ANISOTROPIC MEDIA.* Journal of the Acoustical Society of America, 1991. **90**(2): p. 1106-1118.
44. ROKHLIN, S., T. BOLLAND, and L. ADLER, *REFLECTION AND REFRACTION OF ELASTIC-WAVES ON A PLANE INTERFACE*

BETWEEN 2 GENERALLY ANISOTROPIC MEDIA. Journal of the Acoustical Society of America, 1986. **79**(4): p. 906-918.

45. Damen, E.P.N., et al., *Generation and propagation of coherent phonon beams.* Physical Review B, 2001. **64**(17): p. 174303.
46. Dehoux, T., et al., *Optical tracking of picosecond coherent phonon pulse focusing inside a sub-micron object.* Light: Science &Amp; Applications, 2016. **5**: p. e16082.
47. Ruffin, A., et al., *Direct observation of the Gouy phase shift with single-cycle terahertz pulses.* Physical Review Letters, 1999. **83**(17): p. 3410-3413.
48. Bartels, A., et al., *Ultrafast time-domain spectroscopy based on high-speed asynchronous optical sampling.* Review of Scientific Instruments, 2007. **78**(3): p. 035107.
49. Ranganathan, S.I. and M. Ostoja-Starzewski, *Universal Elastic Anisotropy Index.* Physical Review Letters, 2008. **101**(5): p. 055504.